Slow coarsening of ultra-confined phase-separated glass thin films

B. Bouteille, J. T Fonné, E. Burov, E. Gouillart, H. Henry, H. Montigaud, Pierre Jop, D. Vandembroucq

Slow coarsening of ultra-confined phase-separated glass thin films

B. Bouteille,[1,2] J.T. Fonné,[3] E. Burov,[1] E. Gouillart,[1] H. Henry,[4] H. Montigaud,[1] P. Jop,[1] and D. Vandembroucq[2]
[1)]*Surface du Verre et Interfaces, UMR 125, CNRS/Saint-Gobain, 93303 Aubervilliers, France*
[2)]*PMMH, CNRS, ESPCI Paris, Université PSL, Sorbonne Université, Université de Paris, 75005 Paris, France*[a)]
[3)]*Thin Films Department, Saint-Gobain Research Paris, 39 quai Lucien Lefranc, 93303 Aubervilliers, France*
[4)]*Laboratoire de Physique de la Matière Condensée, Ecole Polytechnique, CNRS, 91128 Palaiseau, France*

(Dated: 3 February 2022)

Diffusion-driven coarsening of droplets is a classical subject in statistical physics, yet coarsening kinetics in confined systems have received little attention. We report here on the coarsening of droplets in thin (50-200 nm) films of phase-separated barium borosilicate glasses. In this ultra-confined geometry where at most one droplet is observed within the film thickness, droplets grow like a power-law of time, with an exponent about 0.17 significantly smaller than the one of Ostwald ripening $(1/3)$, characteristic of bulk coarsening. We complement these experimental results with two-dimensional Cahn-Hilliard numerical simulations of diffusion, where a wider range of parameters can be varied. In simulations in the ultra-confined geometry, we recover a slow coarsening behavior. We explain the anomalous scaling exponent of simulations by the ultraconfined geometry, which imposes a different scaling with time of the radius of a droplet and the distance between droplets. In the experimental system, diffusive transport also becomes less efficient with time compared to the bulk case, with an additional change of geometry compared to simulations. A flattening of droplets with time is indeed observed, which we attribute to strong variations of the diffusion coefficient with the local matrix composition. We finally propose a simple model assuming a spatial localization of the diffusion paths to account for this effect.

In recent years the texturation of thin films has become a major tool to give new functions to material surfaces, such as hydrophobicity[1,2], dew collection[3], anti-reflection[4,5], light absorption[6,7], among many possible applications.

An appealing strategy to obtain and control texturation in thin films and large surfaces is the use of phase separation, a strategy used for example in bio- and bio-inspired materials to achieve structural colors[8–10]. The tuning of the characteristic size of patterns can be achieved via the application of a further step of annealing. It is thus of direct technological interest to understand the kinetics of coarsening of the phase-separated patterns obtained in thin films.

As early predicted by Lifshitz, Slyozhov and Wagner[11,12] (LSW) for the bulk case, the characteristic radius $r(t)$ of a phase-separated droplet is expected to grow as $r(t) \propto t^{1/3}$ with the annealing time t. This result obtained for the case of a diluted droplet actually remains valid for a higher concentration of droplets[13], but also with an inter-connected morphology[14], provided that the transport mechanism is bulk diffusion. The growth law is faster ($r(t) \propto t$) if coarsening is controlled by hydrodynamic transport[15] and slower ($r(t) \propto t^{1/4}$) if it is controlled by surface diffusion on a substrate[16,17].

The LSW scaling is valid in two and three dimensions, and at first sight the thin film geometry could be expected to be innocuous and to only give way to transient regimes. However, the interaction with surfaces and in particular the contrasting wetting properties of the two phases with substrate and atmosphere have been shown to induce a rich and complex phenomenology of the coarsening morphology and its kinetics. The modeling of this phenomenon coined as Surface Directed Spinodal Decomposition (SDSD) has recently been reviewed by Binder et al.[18]. Interestingly, the same authors note that the case where phase separation at walls and in thin films starts by the formation of critical nuclei has received less attention[18]. Zinge-Allmang[19] summarized theoretical models and a handful of experimental or numerical studies[20–22] suggesting long transient regimes and slower coarsening dynamics compared to the bulk case, but also noted that no broad consensus exists because of a scarcity of experimental and numerical studies.

Experimentally, phase separation has become a standard tool to generate ordered patterns in polymer thin films[23,24]. Its use in the context of inorganic thin films was pioneered by Seward et al.[25] in 1968. The development of Physical Vapor Deposition (PVD) techniques have recently triggered progress on the deposition of phase separated thin films of oxide glasses or suboxide materials[4,20,26–30].

Here we report a quantitative study of the coarsening kinetics of droplets in phase-separated barium borosilicate thin films deposited by magnetron sputtering. We report a growth law $r(t) \propto t^{\alpha}$ with a exponent $\alpha \simeq 0.17$, lower than the classical value $\alpha = 1/3$ of the LSW scaling. Using simple scaling arguments and numerical Cahn-Hilliard simulations, we argue in the following that this anomalous slow regime originates from the combination of the confinement and the layered structure of the nucleated droplets.

Our experimental system consists of thin films of barium-borosilicate glass deposited by reactive magnetron sputtering (PVD) on silicon wafers. As shown in Fig. 1a, the barium-borosilicate ternary system has a large immiscibility zone[31–33]. Several studies[34–37] have investigated coarsening kinetics for bulk samples within this ternary system.

[a)]Electronic mail: barbara.bouteille@saint-gobain.com

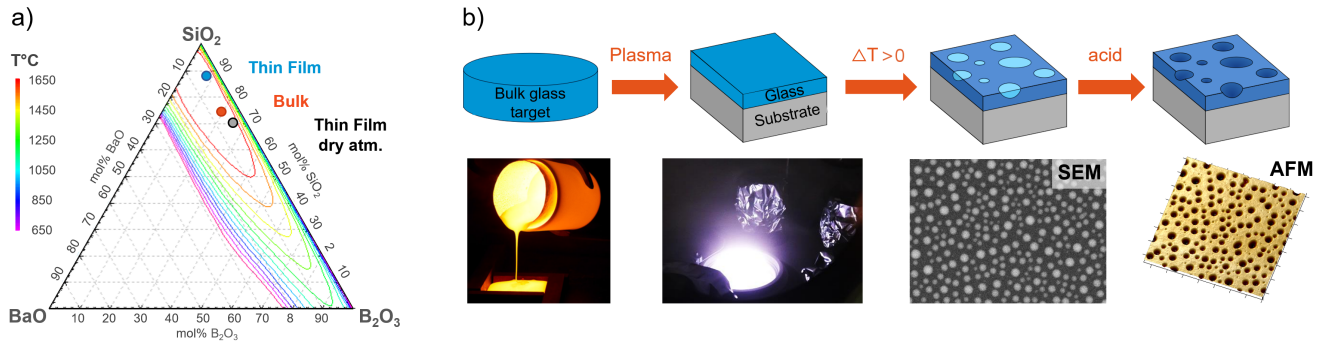

FIG. 1: a) Phase diagram of the ternary glass SiO_2-BaO-B_2O_3. b) Sample preparation: fabrication of the bulk glass as a target to be deposited as a thin layer on a silicon wafer by magnetron sputtering, followed by a thermal treatment triggering the phase separation and the analysis before and after selective etching.

The experimental protocol is summarized in Fig. 1b. A macroscopic target of composition SiO_2-BaO-B_2O_3 75:6:19 mol% was prepared using a traditional melt and quench method. Thin films of thicknesses 45, 90, 98 and 175 nm were deposited on Si wafer substrates inside a custom deposition chamber, using radio-frequency sputtering. Using electron probe microanalysis on several thicker samples, the film composition was measured to be SiO_2-BaO-B_2O_3 88:4:8 mol%. The discrepancy between target and film compositions comes from preferential sputtering of light elements, and a reaction with atmosphere extracting boron from the film to form boric acid. SIMS (Secondary Ion Mass Spectrometry) profiles confirmed that the concentration is homogeneous through the thickness of films.

Samples were annealed under air atmosphere at 950 °C in an electrical furnace. This temperature is a trade-off to limit crystallization at higher temperatures, and to activate molecular diffusion which is an Arrhenian process. Characteristic times of heating and cooling steps were about 2-3 minutes. Annealing times were varied between 1 minute and 32 hours.

Phase-separated films were imaged with Scanning Electron Microscopy (SEM), collecting Back-Scattered Electrons (BSE), using the good contrast between the (bright) barium-rich phase and the other (dark) silica-rich phase. SEM acquisitions were performed on film surface and cross-section, completed by Atomic Force Microscopy (AFM) analysis in tapping mode using tip radius below 10 nm after selective etching of the Barium-rich phase with diluted acidic solution (HF/HNO3). For quantitative image analysis, the Python package scikit-image[38] was used to label pixels from the two phases thanks to a blob-detection algorithm combined with a region-growing step, and to compute the Voronoi cell of each droplet using the random-walker algorithm[39].

In order to test the universality of our experimental results, we have also performed numerical Cahn-Hilliard simulations using a in house code based on a mass conserving scheme using finite differences and explicit forward time-stepping. Details of the model are given in supplemental material A. As shown in Figure 5(a), in order to emulate a thin-film geometry, the simulation is performed in a 2D rectangular domain (of thickness $e = 32, 48, 64$ and lateral size $L = 4096$) with no-flux boundary conditions imposed on the two longest segments, and periodic boundary conditions on the shortest segments. In the initial state a series of Gaussian germs of half-disk geometry (typical radius $r_0 = 6$ with an exclusion distance $\ell_{exc} = 20$)

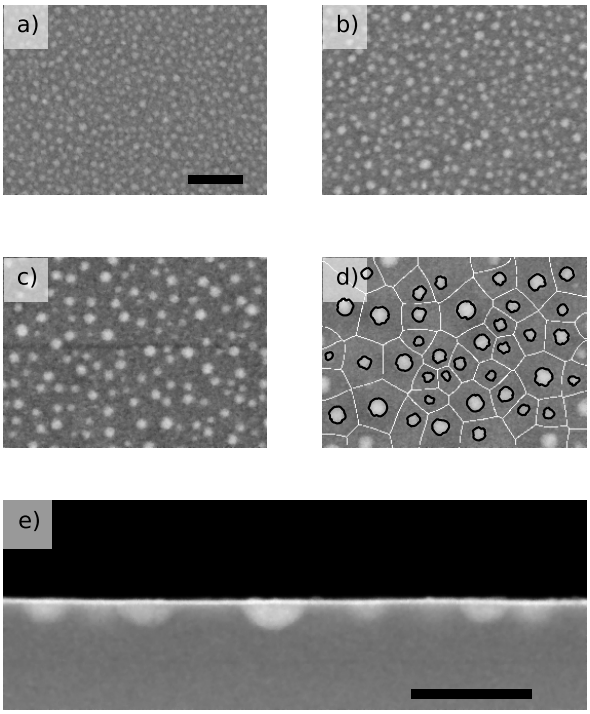

FIG. 2: (a-d) Plane-view SEM images of phase-separated thin films of thickness 45 nm after annealing times of 1 min, 15 min, 120 min and 1200 min at 950 °C. The scale bars represent 250 nm. (d) also shows the contours of segmented droplets and their Voronoi cells. (e) Cross-section SEM image of a phase-separated film of thickness 90 nm after annealing 1200 min at 950 °C. The scale bar represents 250 nm.

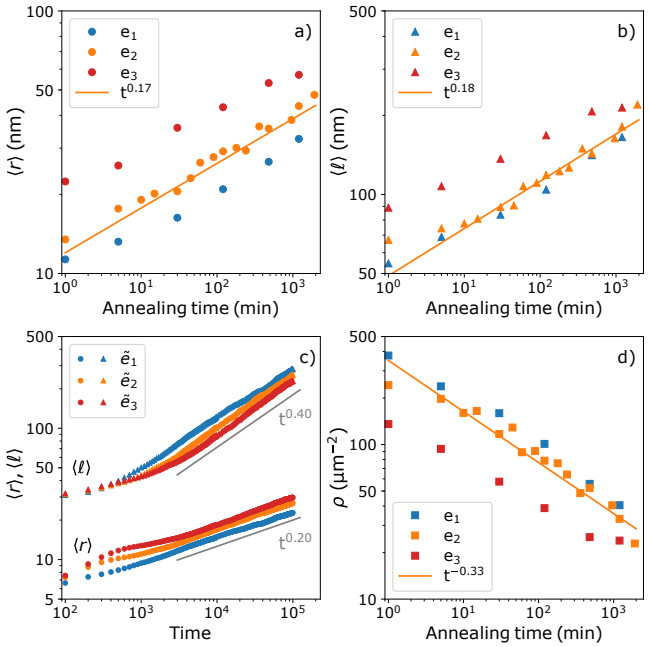

FIG. 3: Kinetics of droplets growth. (a-b-d) **Experiments**: time evolution of (a) average droplet radius r and (b) average distance between droplets ℓ, for three different film thicknesses $e_1 = 45$ nm, $e_2 = 98$ nm and $e_3 = 175$ nm, with power-law least-squares fits for e_2. (d) Time evolution of the surface density of droplets, for the three experimental film thicknesses. (c) **Simulations**: same as (a-b) for Cahn-Hilliard simulations of droplet coarsening in thin films of three thicknesses $\tilde{e}_1 = 32$, $\tilde{e}_2 = 48$ and $\tilde{e}_3 = 64$, with droplets initialized at the surface of the film.

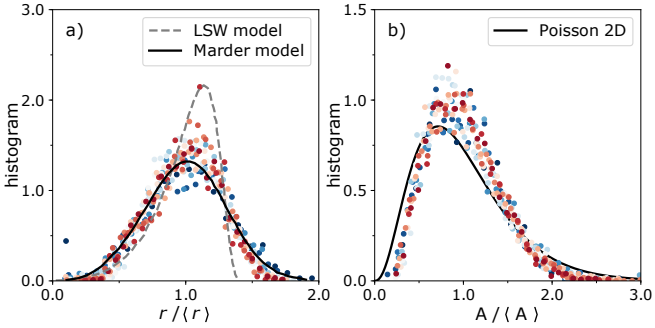

FIG. 4: (a) Histogram of droplet radius r normalized by average radius for 16 annealing times between one minute (dark blue) and 1920 minutes (red) at 950 °C for the film thickness of 98 nm (see Fig. 2(a)). Theoretical distributions for the LSW model (ultra-diluted limit) and the Marder model (with correlations between neighbors) are shown for comparison. (b) Histogram of normalized areas of Voronoi cells $\mathscr{A}$, for the same annealing times as in (a). The distribution of Voronoi areas for a Poisson distribution[41] is shown for comparison.

are implemented at the surface[40].

We show in Fig. 2 plane-view and cross-section SEM images of phase-separated thin films at different annealing times, for a film thickness of 45 nm and 90 nm. A droplet morphology is observed. Cross-section images show (Fig. 2 (e)) that most (almost all) droplets touch the surface. A similar morphology is observed for the other two thicknesses: at most one droplet is observed within the thickness of the glass film, a situation which we call *ultra-confined geometry*.

In Fig. 2 (a-d) SEM images also show that both the average diameter of droplets and their average distance increase with annealing time. In order to study quantitatively this growth phenomenon, we draw in Fig. 2 (d) the contour of the droplets and the associated Voronoi cells. This allows us to define two characteristic length scales: $r(t) = \langle\sqrt{\mathscr{A}_{droplet}}\rangle$ is an average radius of the droplets where $\mathscr{A}_{droplet}$ is the area of one droplet and brackets denotes an ensemble average; $\ell(t) = \langle\sqrt{\mathscr{A}_{Voronoi}}\rangle$ is a typical distance between neighboring droplets where $\mathscr{A}_{Voronoi}$ is the area of a Voronoi cell.

In Fig. 3 (a-b) we have plotted the evolution with time of the two length scales $r(t)$ and $\ell(t)$, in logarithmic coordinates and for three different film thicknesses. In both cases, a power-law behavior is observed over the almost three time decades of the temporal range: $r(t) \propto t^{\alpha_r}$ and $\ell(t) \propto t^{\alpha_\ell}$. For the three time series, least-square fits give for the exponents $\alpha_r = 0.17$ and $\alpha_\ell = 0.18$. Note that these values are significantly smaller than the classical LSW exponent of Ostwald ripening, $\alpha_{LSW} = 1/3$.

In Fig. 4 we show the histogram of the characteristic radius $r(t)$ and of the area $\mathscr{A}(t)$ of the Voronoi cells. In rescaled coordinates, it appears clearly that in both cases the histograms obtained at different times of the annealing process superimpose onto a unique master curve. The droplet pattern remains therefore invariant after dynamic rescaling. Furthermore, while the histogram of droplet radii is quite different from the one of the LSW model, corresponding to a diluted limit, it is in quite good agreement with the model of Marder which takes into account correlations between neighbors[13]. More specifically, Marder introduces an interaction between a particle and its shell of first neighbors. The length of this shell defines a so-called screening length, a cut-off beyond which interactions are not taken into account. As for the histogram of Voronoi areas, it is more peaked than a Poisson model obtained with randomly distributed points[41], implying that there exists an exclusion distance between droplets.

As noted by Binder *et al*[18], the kinetics of phase separation in confined geometries still remains a challenging problem of nonequilibrium statistical mechanics. In the present case, even though we measured exponents that differ from the classical LSW prediction, the validity of dynamic scaling encourages us to analyze the power-law behavior of $r(t)$ and $\ell(t)$ as a genuine scaling regime and not as a simple transient. In the following, we adapt the classical scaling arguments for LSW coarsening[42,43] to the ultraconfined geometry.

In bulk geometry, mass conservation induces an immediate (trivial) scaling relation between the characteristic radius $r(t)$ of a spherical droplet and the typical distance $\ell(t)$ that sepa-

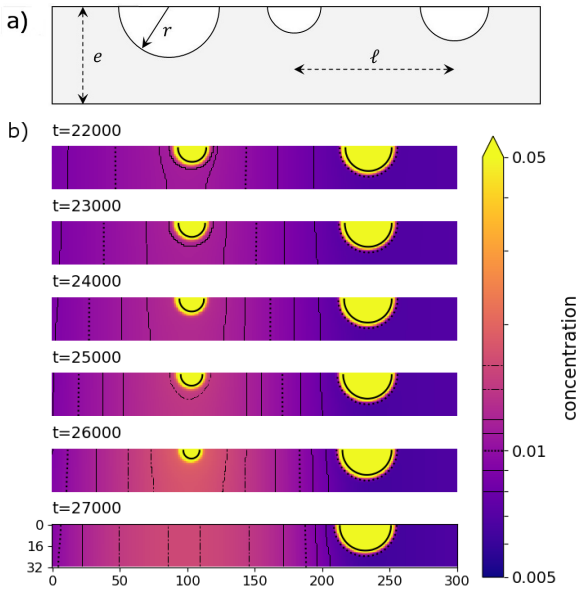

FIG. 5: (a) Sketch of the spatial organization of droplets in an "ultra-confined" thin layer geometry, introducing the different length scales: r is the droplet radius, ℓ the distance between droplets, and e the thickness of the layer. (b) Concentration field resulting from the evaporation of a droplet, displayed using a logarithmic colorscale. The isovalue lines are 0.008, 0.009, 0.01 (bold dotted lines), 0.011, 0.012, then 0.014 and 0.016 (dashed lines).

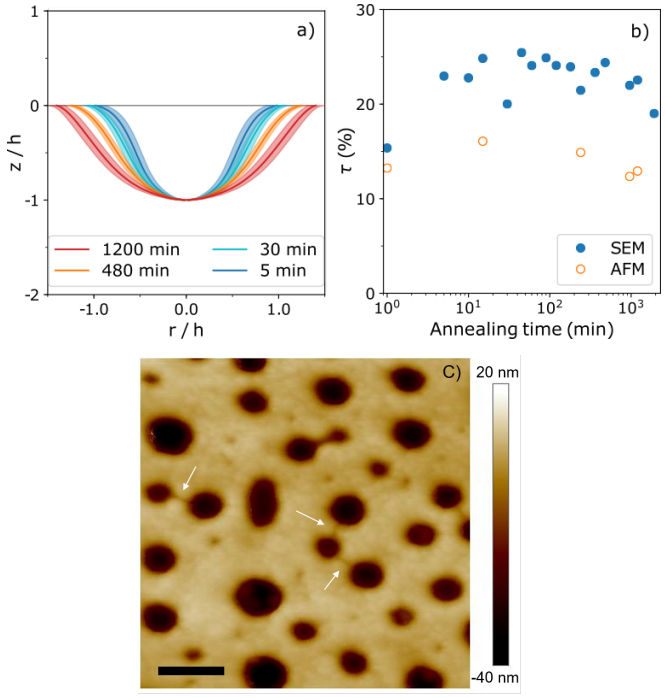

FIG. 6: (a) Average normalized shape of droplets measured by AFM at different times. (b) Fraction of surface covered by droplets, measured for the same sample (98 nm) from SEM and AFM images. The difference between the two measurements is attributed mainly to AFM-tip artifacts. (c) AFM image of sample 90 nm after 30 min annealing, and after chemical etching. Arrows indicate thin rifts revealed by selective chemical etching, which are interpreted as a local barium over-concentration. The scale bar represents 100 nm.

rates two neighboring droplets:

$$\frac{[r(t)]^d}{[\ell(t)]^d} \approx \phi \quad \Rightarrow \quad r(t) \approx \phi^{1/d}\ell(t)\,, \tag{1}$$

where d is the space dimension and ϕ the volume fraction of the minority phase in the bulk.

The proportionality between these two length scales $r(t)$ and $\ell(t)$ breaks down in the present case of ultra-confinement since droplets are expected to grow as in bulk (3D) while they can only go further apart along the surface (2D):

$$\frac{[r(t)]^d}{e[\ell(t)]^{d-1}} \approx \phi \quad \Rightarrow \quad r(t) \approx \phi^{1/d} e^{1/d} \ell(t)^{\frac{d-1}{d}}\,, \tag{2}$$

where e is the thickness of the thin film. We thus get $\ell \propto r^2$ in 2D and $\ell \propto r^{3/2}$ in 3D.

On the other hand, concentration fields obtained numerically show that the concentration gradient is mostly parallel to the free surface (see Fig. 5). Therefore mass conservation of material diffusing between droplets writes:

$$\frac{\mathrm{d}v}{\mathrm{d}t} \propto SJ\,, \tag{3}$$

where $v \propto r^d$ is the volume of a droplet and S is a diffusion cross-section. The one-dimensional flux value J is estimated using Fick's law

$$J = D\frac{\delta c}{\ell}\,. \tag{4}$$

Here D is a diffusion coefficient associated to the mobility of the most mobile species of our ternary diagram, which is barium, a network modifier. Since both phases have a large silica content, and approximately the same boron oxide content, coarsening is controlled by the exchange of barium between droplets, which is mediated by atomic diffusion through the matrix phase.. The typical scale for the concentration gradient is chosen as ℓ. Here ℓ is equivalent to the "screening length" which has been introduced by theoretical models of coarsening in films[13,19], which showed that the screening length is of the order of the inter-droplet distance ℓ. As for the cross-section S, we propose that it corresponds to the boundary of the Voronoi cell, leading to $S = e\ell^{d-2}$. Combining the above equations with the usual assumption that $\delta c \propto \gamma/r$ where γ is the surface tension and integrating the differential equation results for the 2-d case of simulations in:

$$r(t) \propto t^{1/5}. \tag{5}$$

The scalings obtained from this simple geometrical model are in good agreement with numerical results both for $r(t) \propto t^{\frac{1}{5}}$ and $\ell(t) \propto r^2(t) \propto t^{2/5}$ (see Fig. 3 (c)). This means that the ultra-confined geometry is enough to result in a slow coarsening regime.

Nevertheless, our *experimental* observations suggest that ℓ and r are proportional. Therefore, the scaling relation induced by mass conservation (Eq. 2) for ultra-confined spherical droplets is not respected. Rather, accounting for the proportionality between ℓ and r, mass conservation implies that the droplet volume scales as $v \propto r^2$. In particular the shape of droplets must change with time. In Fig. 6 (a), we have plotted the average shape of droplets obtained from AFM measurements for different annealing times and after the chemical etching of the barium-rich phase. These profiles were obtained by computing an angular average of the depth profile for each droplet, normalizing it by the depth of the droplet, and finally averaging these normalized profiles over several tens of droplets measured in AFM images. We observe that droplets become flatter with larger annealing times, explaining why it is possible to almost conserve the total surface of the barium-rich phase (implied by the proportionality between ℓ and r, and directly measured in Fig. 6 (b)).

The evolution of the shape of droplets with time is a surprising result, implying in particular that either the contact angle at the surface between the two phases also evolves with time, or that the curvature is not constant along the droplet surface. However, the diffusion of barium in the matrix is expected to depend strongly on the local chemical composition of the matrix[37,44,45], with an exponential dependence of the diffusion coefficient with the silica concentration[46,47]. Therefore, we expect that diffusion between droplets will be faster along specific paths where the barium concentration is higher, in particular, along segments linking droplets together at the surface. The topography revealed by preferential chemical etching of barium in Fig. 6 (c) shows small rifts along such segments, in agreement with the hypothesis of preferential diffusion paths with a higher barium concentration. Concentration gradients within the matrix could result in a gradient of interfacial tension γ between the droplet composition and the local matrix composition, and hence in variations of the local curvature without pressure gradient inside the droplet (constant γ/r ratio).

Still one may try to rewrite the previous scaling arguments to account for a spatial heterogeneity of the diffusion paths. Keeping unchanged the estimate of the flux J given in Eq. (4) we rewrite Eq. (3), assuming now a platelet shape of the droplet $v(t) \propto r_0 r(t)^2$ (where r_0 is a typical radius) and a time independent cross section $S \propto r_0^2$. Here we consider that the length scale r_0 gives also the characteristic width of the diffusion paths (corresponding to the small rifts visible in Fig. 6c). Accounting for this diffusion paths hypothesis, we now get:

$$\frac{d}{dt}\left[r_0 r(t)^2\right] \propto r_0^2 D \frac{\gamma}{\left[r(t)^2\right]}\,, \tag{6}$$

where we also assumed the proportionality $\ell(t) \propto r(t)$. This leads asymptotically to $r(t) \propto t^{1/4}$. Together with the geometrical confinement the hypothesis of a strong localization of the diffusion paths thus seems to induce a coarsening slower than the LSW law. This crude model certainly requires to be tested more seriously. Numerical models incorporating these ingredients (diffusivity and interfacial tension depending on the local matrix composition) are beyond the scope of this study, but could shed light on the specific coarsening dynamics in phase-separated silicate films.

We identified that slow droplet coarsening, with exponents lower than $1/3$, are an intrinsic characteristic of the ultra-confined geometry of thin phase-separated films, where only one droplet is found in the film thickness. Numerically we could identify a key geometrical ingredient of this slow coarsening: the decoupling between the distance between droplets and the radius of droplets. Droplets are further and further from each other with annealing time in this geometry, resulting in less efficient diffusive transport. In the experimental case of silicate thin films, along with the confinement, a change of droplet geometry with time is measured, with flatter droplets as time increases. Qualitatively, we attributed this change of aspect ratio to the strong dependence of the diffusion coefficient with the local matrix composition and could propose a simple model of slow coarsening based upon geometrical confinement and localized diffusion paths

We gratefully acknowledge the help of Bruno Bresson and Anne Lelarge for AFM measurements, and of Erick Lamotte and Johnny Vallon for bulk glass elaboration. This work was funded thanks to a joint Ph.D. grant of Agence Nationale Recherche et Technologie and Saint-Gobain Research Paris.

[1] A. Nakajima, K. Abe, K. Hashimoto, and T. Watanabe, "Preparation of hard super-hydrophobic films with visible light transmission," Thin Solid Films **376**, 140–143 (2000).

[2] A. Dubov, K. Perez-Toralla, A. Letailleur, E. Barthel, and J. Teisseire, "Superhydrophobic silica surfaces: fabrication and stability," J. Micromech. Microeng. **23**, 125013 (2013).

[3] T. Mouterde, G. Lehoucq, S. Xavier, A. Checco, C. T. Black, A. Rahman, T. Midavaine, C. Clanet, and D. Quéré, "Antifogging abilities of model nanotextures," Nat. Mater. **16**, 658–663 (2017).

[4] T. Aytug, A. R. Lupini, G. E. Jellison, P. C. Joshi, I. H. Ivanov, T. Liu, P. Wang, R. Menon, R. M. Trejo, E. Lara-Curzio, S. R. Hunter, J. T. Simpson, M. P. Paranthaman, and D. K. Christen, "Monolithic graded-refractive-index glass-based antireflective coatings: broadband/omnidirectional light harvesting and self-cleaning characteristic," J. Mater. Chem. C **3**, 5440 (2015).

[5] A. Rahman, A. Ashraf, H. Xin, X. Tong, P. Sutter, M. D. Eisaman, and C. T. Black, "Sub-50-nm self-assembled nanotextures for enhanced broadband antireflection in silicon solar cells," Nat. Commun. **6**, 1–6 (2015).

[6] M. Aeschlimann, T. Brixner, D. Differt, U. Heinzmann, M. Hensen, C. Kramer, F. Lükermann, P. Melchior, W. Pfeiffer, M. Piecuch, C. Schneider, H. Stiebig, C. Strueber, and P. Thielen, "Perfect absorption in nanotextured thin films via anderson-localized photon modes," Nat. Photonics **9**, 663–668 (2015).

[7] P. Jacquet, B. Bouteille, R. Dezert, J. Lautru, R. Podor, A. Baron, J. Teisseire, J. Jupille, R. Lazzari, and I. Gozhyk, "Periodic arrays of diamond-shaped silver nanoparticles: From scalable fabrication by template-assisted solid-state dewetting to tunable optical properties," Adv. Funct. Mater. **29**, 1901119 (2019).

[8] E. R. Dufresne, H. Noh, V. Saranathan, S. G. Mochrie, H. Cao, and R. O. Prum, "Self-assembly of amorphous biophotonic nanostructures by phase separation," Soft Matter **5**, 1792–1795 (2009).

[9] S. L. Burg, A. Washington, D. M. Coles, A. Bianco, D. McLoughlin, O. O. Mykhaylyk, J. Villanova, A. J. C. Dennison, C. J. Hill, P. Vukusic, S. Doak, S. J. Martin, M. Hutchings, S. R. Parnell, C. Vasilev, N. Clarke, A. J. Ryan, W. Furnass, M. Croucher, R. M. Dalgliesh, S. Prevost, R. Dattani, A. Parker, R. A. L. Jones, J. P. A. Fairclough, and A. J. Parnell, "Liquid-liquid phase separation morphologies in ultra-white beetle scales and a synthetic equivalent," Comm. Chem. **2** (2019), 10.1038/s42004-019-0202-8.

[10] H. Wang, Y. Liu, Z. Chen, L. Sun, and Y. Zhao, "Anisotropic structural color particles from colloidal phase separation," Sci. Adv. **6**, eaay1438 (2020).

[11] I. M. Lifshitz and V. V. Slyozov, "The kinetics of precipitation from supersaturated solid solutions," J. Phys. Chem. Solids **19**, 35–50 (1961).

[12] C. Wagner, "Theorie der Alterung von Niederschlägen durch Umlösen (Ostwald-Reifung)," Z. Elektrochem. **65**, 581–591 (1961).

[13] M. Marder, "Correlations and ostwald ripening," Phys. Rev. A **36**, 858 (1987).

[14] D. Dalmas, A. Lelarge, and D. Vandembroucq, "Quantitative AFM measurements on phase separated glass surfaces," J. Non-Cryst. Solids **353**, 4672–4680 (2007).

[15] E. D. Siggia, "Late stages of spinodal decomposition in binary mixtures," Phys. Rev. A **20**, 595 (1979).

[16] B. Chakraverty, "Grain size distribution in thin films - 1. conservative systems," J. Phys. Chem. Solids **28**, 2401–2412 (1967).

[17] K. Shorlin, S. Krylov, and M. Zinke-Allmang, "Fundamental problems concerning three dimensional clustering on surfaces," Physica A: Statistical Mechanics and its Applications **261**, 248–265 (1998).

[18] K. Binder, S. Puri, S. K. Das, and J. Horbach, "Phase separation in confined geometries," J. Stat. Phys. **138**, 51–84 (2010).

[19] M. Zinke-Allmang, "Phase separation on solid surfaces: nucleation, coarsening and coalescence kinetics," Thin Solid Films **346**, 1–68 (1999).

[20] C. Hwang, J. Kim, B. K. Ryu, and H. Takebe, "Preparation of porous glass films using phase separation phenomenon and growth behavior of phase-separated structure," J. Mater. Sci. **48**, 8068–8076 (2013).

[21] H. Gidituri, S. V. D. Vijay Anand, and M. V. PanchagnulaHarinadha, "Dissipative particle dynamics study of phase separation in binary fluid mixtures in periodic and confined domains," J. Chem. Phys. **147**, 074703 (2017).

[22] H. Wang and R. J. Composto, "Thin film polymer blends undergoing phase separation and wetting: Identification of early, intermediate, and late stages," The Journal of Chemical Physics **113**, 10386 (2000).

[23] L. Xue, J. Zhang, and Y. Han, "Phase separation induced ordered patterns in thin polymer blend films," Prog. Polymer Sci. **37**, 564–594 (2012).

[24] S. Reich and Y. Cohen, "Phase separation of polymer blends in thin films," J. Pol. Sci. Pol. Phys. **19**, 1255–1267 (1981).

[25] T. P. Seward III, D. R. Uhlmann, and D. Turnbull, "Development of two-phase structure in glasses, with special reference to the system BaO-SiO_2," J. Amer. Ceram. Soc. **51**, 634 (1968).

[26] F. Utsuno, H. Mori, H. Inoue, and I. Yasui, "Phase separation of Na_2O–SiO_2 films prepared by sputtering," J. Non-Cryst. Solids **349**, 337–340 (2004).

[27] T. Aytug, J. T. Simpson, A. R. Lupini, R. M. Trejo, G. E. Jellison, I. N. Ivanov, S. J. Pennycook, D. A. Hillesheim, K. O. Winter, D. K. Christen, S. R. Hunter, and J. A. Haynes, "Optically transparent, mechanically durable, nanostructured superhydrophobic surfaces enabled by spinodally phase-separated glass thin films," Nanotechnology **24**, 315602 (2013).

[28] P. Martin, A. Bendavid, K. H. Mueller, and L. Randeniya, "Mesoporous surfaces by phase separation of Al–Si thin films," Thin Solid Films **528**, 175 (2013).

[29] M. Roussel, E. Talbot, C. Pareige, R. P. Nalini, F. Gourbilleau, and P. Pareige, "Confined phase separation in sio_x nanometric thin layers," Appl. Phys. Lett. **103**, 203109 (2013).

[30] G. Beainy, J. Weimmerskirch-Aubatin, M. Stoffel, M. Vergnat, H. Rinnert, C. Castro, P. Pareige, and E. Talbot, "Structural and optical study of ce segregation in ce-doped sio1. 5 thin films," J. Appl. Phys. **118**, 234308 (2015).

[31] E. M. Levin and G. M. Ugrinic, "The system barium oxide-boric oxide-silica," J. Res. Nat. Bur. Stand. **25**, 47–53 (1953).

[32] E. Levin and S. Block, "Structural interpretation of immiscibility in oxide systems: I, analysis and calculation of immiscibility," J. Am. Ceram. Soc. **40**, 95–106 (1957).

[33] W. Vogel, "Phase separation in glass," J. Non-Cryst. Solids **25**, 170–214 (1977).

[34] D. Bouttes, E. Gouillart, E. Boller, D. Dalmas, and D. Vandembroucq, "Fragmentation and Limits to Dynamical Scaling in Viscous Coarsening: An Interrupted in situ X-Ray Tomographic Study," Phys. Rev. Lett. **112**, 245701 (2014).

[35] D. Bouttes, O. Lambert, C. Claireaux, W. Woelffel, D. Dalmas, E. Gouillart, P. Lhuissier, L. Salvo, E. Boller, and D. Vandembroucq, "Hydrodynamic coarsening in phase-separated silicate melts," Acta Mater. **92**, 233–242 (2015).

[36] D. Bouttes, E. Gouillart, and D. Vandembroucq, "Topological symmetry breaking in viscous coarsening," Phys. Rev. Lett. **117**, 145702 (2016).

[37] Y. Gueguen, P. Houizot, F. Célarié, M. Chen, A. Hirata, Y. Tan, M. Allix, S. Chenu, C. Roux-Langlois, and T. Rouxel, "Structure and viscosity of phase-separated BaO–SiO_2 glasses," J. Am. Ceram. Soc. **100**, 1982–1993 (2017).

[38] S. van der Walt, J. L. Schönberger, J. Nunez-Iglesias, F. Boulogne, J. D. Warner, N. Yager, E. Gouillart, and T. Yu, "scikit-image: image processing in Python." PeerJ **2**, e453 (2014).

[39] L. Grady, "Random walks for image segmentation." IEEE transactions on pattern analysis and machine intelligence **28**, 1768–83 (2006).

[40] B. Bouteille, *Séparation de phase dans les couches minces de verre pour la nanostructuration de surface*, Theses, Sorbonne Université (2020).

[41] J.-S. Ferenc and Z. Néda, "On the size distribution of Poisson Voronoi cells," Physica A: Statistical Mechanics and its Applications **385**, 518–526 (2007).

[42] D. A. Huse, "Corrections to late-stage behavior in spinodal decomposition: Lifshitz-Slyozov scaling and Monte Carlo simulations," Phys. Rev. B **34**, 7845–7850 (1986).

[43] A. J. Bray, "Theory of phase-ordering kinetics," Adv. Phys. **43**, 357–459 (1994).

[44] J.-T. Fonné, E. Burov, E. Gouillart, S. Grachev, H. Montigaud, and D. Vandembroucq, "Interdiffusion between silica thin films and soda-lime glass substrate during annealing at high temperature," J. Am. Ceram. Soc. **102**, 3341–3353 (2019).

[45] C. Claireaux, M.-H. Chopinet, E. Burov, H. Montigaud, M. Roskosz, M. J. Toplis, and E. Gouillart, "Influence of temperature on multicomponent diffusion in calcium and sodium aluminosilicate melts," J. Non-Cryst. Solids **505**, 170–180 (2019).

[46] J. E. Mungall, "Empirical models relating viscosity and tracer diffusion in magmatic silicate melts," Geochim. Cosmochim. Ac. **66**, 125–143 (2002).

[47] Y. Zhang, H. Ni, and Y. Chen, "Diffusion Data in Silicate Melts," Rev. Mineral. **72**, 311–408 (2010).

[48] J. W. Cahn and J. E. Hilliard, "Free Energy of a Nonuniform System. I. Interfacial Free Energy," The Journal of Chemical Physics **28**, 258 (1958).

SUPPLEMENTARY MATERIAL

A. The Cahn Hilliard Model

In this subsection we present in more details the Cahn-Hilliard model used here and discuss the parameters used and the link between them and physical quantities. The Cahn Hilliard model used was introduced and studied in[48]. It is based on a conservation equation:

$$\partial_t c = \nabla(M\nabla\mu) \tag{7}$$

where c is a linear function of concentration, M is the mobility and μ is the chemical potential. μ is to the functional derivative of a free functional energy that writes:

$$\mathscr{F} = \gamma \int \frac{1}{\kappa} c^2(1-c)^2 + \kappa(\nabla c)^2 \tag{8}$$

where γ is a parameter that is proportional to the surface tension whereas κ is a parameter that is proportional to the interface thickness. The function $c^2(1-c)^2$ is a simple double well potential with a common tangent in $c=1$ and $c=0$. This model has for equilibrium solutions front between $c=0$ and $c=1$, the points on the common tangent. The front solution writes:

$$c = \frac{1}{2}\left(1+\tanh(\frac{x}{\sqrt{2}\kappa}\right). \tag{9}$$

This front has a thickness proportional to κ and the excess energy (the surface tension) associated with the front is $\gamma\sqrt{2}/6$. Finally the diffusion coefficient in either one or the other phase is with the model used here:

$$D = \frac{2M}{\kappa} \tag{10}$$

In our simulations we have used $\gamma = 1$ and $\kappa = 1$ while the mobility was taken $M = 4$. The grid spacing was equal to 1 and the time step to 0.01.

This choice is arbitrary but it has not any consequence on the physics as long as the interface thickness is much smaller than the characteristic size of the studied patterns. Indeed in this case, it has been shown that the deviation of equilibrium concentration close to a curved interface (which is the driving force for coarsening) is a function of γ/r with r the radius of curvature of the interface and is independent of the interface thickness. Since this work is focused on scaling laws during a self similar regime, the results obtained are robust with respect to both time and space rescaling and are independent of the parameters used which solely affect the prefactors of the scaling laws.

B. Distribution of radii in the simulations

We measured the distributions of radius of the droplets normalized by the mean radius in the numerical simulations. The results are presented in the Figure 7 for the early time ($t = 200$) and later times ($t > 10^4$). In the very first time, while all the numerical seeds have the same radius, the distributions broaden quickly toward a gaussian-like shape. Those distributions superimposed on each other for different values of thicknesses. Also when the ripening regime is obtained after a short transient, the distributions collapse on a master curve for all times, underlining the self-similarity of the distributions. In these confined 2D simulations, this master curve is closer to the LSW prediction (line).

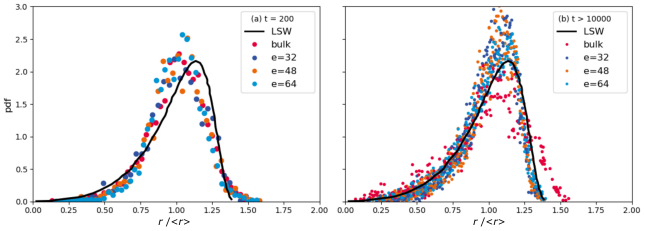

FIG. 7: Histogram of the droplet radius r normalized by the average radius for early time $t = 200$ (a) and for all the time greater than 10^4 (b). The red dots correspond to bulk 2D simulations, the other dots to $e = 32$, 48, and 64. The line shows the LSW prediction for the distribution of radius. We excluded from this analysis the rare droplets touching both boundaries.